CINTAL - Centro de Investigação Tecnológica do Algarve

Universidade do Algarve

BIOCOM'19 experiment data report: particle motion measurements

S.M.Jesus, L. Maia, F. Xavier, R. Vio and E. Vale

Rep 02/19 - SiPLAB
Date: 30/October/2019

University of Algarve
Campus de Gambelas
8005-139, Faro
Portugal

tel: +351-289800131
fax: +351-289864258
cintal@ualg.pt
www.ualg.pt/cintal

Work requested by	IEAPM, under CsF project BIOCOM
Laboratory performing the work	SiPLAB - Signal Processing Laboratory FCT, Campus de Gambelas, Universidade do Algarve, 8005-139 Faro, Portugal tel: +351-289800949 info@siplab.uceh.ualg.pt, www.siplab.fct.ualg.pt
Project	BIOCOM
Title	BIOCOM'19 experiment data report: particle motion measurements
Authors	S.M.Jesus, L. Maia, F. Xavier, R. Vio and E. Vale
Date	October 30, 2019
Reference	02/19 - SiPLAB
Number of pages	40 (forty)
Abstract	This document briefly describes the experiment that took place at the "Enseada de Cabo Frio", Arraial do Cabo (RJ, Brasil), between 14 and 18th January, 2019, focusing on the Dual Accelerometer Vector Sensor (DAVS) installation, setup and data acquisition. It also reports preliminary results obtained on the data acquired on the DAVS receiver, and anticipates the effect of particle motion due to anthropogenic activities on the biologically rich community of the rocky shore of the "fenda da Nossa Senhora" and Boqueirão of Cabo Frio Island.
Clearance level	NON CLASSIFIED
Distribution list	SiPLAB, IEAPM, CINTAL
Attached	None
Total number of recipients	3 (three)

Approved for publication

A.B. Ruano

President Administration Board

Foreword and Acknowledgment

This work was performed during the 30-day stay at IEAPM in January 2019, in the framework of the Research Visiting program, foreseen under project BIOCOM, funded by the CsF program (Brasil). The data was acquired during the BIOCOM'19 experiment. The authors would like to thank the project coordinator Eduardo Netto and Acoustics Group coordinator Marcus V. Simões, as well as all BIOCOM'19 experiment participants and, in particular, Fábio Xavier, Renato Vio, Jefferson Ostrovsky, Lussac Maia, Fábio Louza, Vicente Barroso and Eduardo Vale, and the support of the technical and on board personnel for the preparation and running of the experiment.

intentionally blank

Contents

List of Figures

intentionally blank

Abstract

This document briefly describes the experiment that took place at the "Enseada de Cabo Frio", Arraial do Cabo (RJ, Brasil), between 14th and 18th January, 2019, focusing on the Dual Accelerometer Vector Sensor (DAVS) installation, setup and data acquisition. It also reports preliminary results obtained on the data acquired on the DAVS receiver, and anticipates the effect of particle motion due to anthropogenic activities on the biological rich community of the rocky shore of the "fenda da Nossa Senhora" and Boqueirão of Cabo Frio Island.

intentionally blank

Chapter 1

Introduction

Early studies have reported important differences between the sound pressure and acoustic particle motion field at low frequencies and its possible separate effects on fish with lateral line organs or other mechanoreceptors [3]. It was suggested that the particle motion driven field could mask the ambient noise field at close range and low frequency. More recently several particle motion measurements were conducted during the installation and operation of wind turbines and the potential impact of fish [4, 5]. The hearing mechanism of fish and invertebrates has been abundantly described in the literature focusing, more recently, on the often underestimated sensitivity of marine organisms to particle motion [6]. Therefore the motivation for performing particle velocity measurements during the BIOCOM'19 sea trial was twofold: a) to determine differences between sound pressure and particle motion due to anthropogenic activities due to recreational boating and coastal sightseeing and b) to compare sound pressure and particle motion biological signatures during anthropogenic noise free periods.

The Dual Accelerometer Vector Sensor - version 1 (DAVS1) was developed at CINTAL [7] during the EU H2020 WiMUST project[1] as a device for sensing acoustic particle velocity in AUV-based seismic applications [8] and is covered by a pending international patent[2]. During BIOCOM'19 the DAVS1 was used for the characterization of the particle motion bioacoustic activity and the impact of anthropogenic noise generated by typical summer boating activities.

[1]funded under contract ICT-645141 of the European Union under H2020 research program between 2015 and 2018.

[2]submitted patent number PT110003, 2018.

Chapter 2

Background on data analysis

This section gives some background for the processing of the DAVS data set. As its name indicates the dual accelerometer vector sensor (DAVS) has two closely spaced accelerometers and one hydrophone. Since each accelerometer is tri-axial, the recorded acoustic data includes seven channels as follows:

- two tri-axial accelerometers: #49 and #50, producing six information channels with acoustic particle accelerations, labeled as Ax49, Ay49, Az49, Ax50, Ay50 and Az50, along x, y, and z axis, respectively;
- one acoustic pressure channel labeled Prs.

Data files recorded on disk are first converted to input physical quantities, both for the acoustic particle acceleration [m/s^2] and the sound pressure [μPa], by taking into account the various chain gains and sensor sensitivities (see section 4 and annex A.1).

In the sequel we will use two types of representations: one direct where acoustic pressure received on the hydrophone is displayed along side the various particle acceleration channels and another where acceleration is converted to velocity and then to pressure equivalent particle velocity so it can be represented in the same units as acoustic pressure and, in case, combined with it.

2.1 Acceleration and pressure

The most common form for showing acceleration and pressure is in the frequency domain, through spectrograms, power spectral densities and power spectrum estimates.

Spectrograms allow for representing spectral content evolution through time using Short Time Fourier Transforms (STFT) which, if displayed in power units, are power sample spectra taken at each time frame. If appropriately scaled by the energy of the weighting window (if any) and by the time window duration, these would be samples of power spectral density (PSD) or power spectrum (PS) [9]. The former would generally show lower levels since the energy is spread through the frequency bin width, while in the later the power value at each discrete frequency would be directly proportional to the received power at that frequency (see details in [9] and [10]).

In order to obtain stable PSD and PS estimates, averaging is generally performed over a given time window. This is performed by a simple average of the STFT.

Acceleration PSD is represented in [dB // (m s^{-2})^2/Hz] while acceleration PS is averaged over frequency bin so it will be given in [dB // (m s^{-2})^2]. Instead acoustic pressure PSD will classically be given in [dB // (μPa)^2/Hz] and pressure PS in [dB // (μPa)^2] (see [9] for discussion regarding the ratio of acoustic intensities and pressures).

2.2 Pressure equivalent conversion

In order for the various channels to be displayed in similar meaningful scales acoustic particle accelerations may be converted to particle velocity and then to pressure equivalent particle velocity. This is done as follows.

Particle displacement $m(x,t)$, for example, along axis x and at time t is related to particle velocity $v(x,t)$ and particle acceleration $a(x,t)$ through successive differentiation relative to time according to

$$v(x,t) = \frac{\partial m(x,t)}{\partial t}, \qquad a(x,t) = \frac{\partial v(x,t)}{\partial t} \tag{2.1}$$

or in the frequency domain

$$V(x,\omega) = j\omega M(x,\omega), \qquad A(x,\omega) = j\omega V(x,\omega) \tag{2.2}$$

For frequencies above the cut-off frequency set by

$$f_{\text{cut-off}} = \frac{c(\pi - \rho_{\text{sed}}/\rho_{\text{water}})}{2\pi H \sin(\arccos(c/c_{\text{sed}}))}, \tag{2.3}$$

where ρ_{sed}, c_{sed} and ρ, c are the densities and sound speed in the sediment and in the water, respectively, and H is the water depth, the acoustic field supports plane-wave solutions for the wave equation and therefore one may assume that the velocity potential, for example along axis x, $\phi = f(x - ct)$, is some travelling wave, function of x and t. According to the Euler's equation we have that

$$\frac{\partial p}{\partial x} = -\rho\frac{\partial v_x}{\partial t} = -\rho\frac{\partial^2 \phi}{\partial x \partial t} \tag{2.4}$$

since $v_x = \partial\phi/\partial x$, so that integrating for x on both sides

$$p = -\rho\frac{\partial \phi}{\partial t} = \rho c f'(x - ct) \tag{2.5}$$

and therefore using the fact that according to $\mathbf{v} = \nabla\phi$, *i.e.*, that $v_x = f'(x - ct)$ we can write *the fundamental relation connecting sound pressure equivalent and particle velocity* for plane waves

$$v_p = \rho c v \tag{2.6}$$

where v is the scalar particle velocity. At short range r from source the approximate relation is used [11]

$$v_p = \rho c v \left(1 + \frac{\lambda}{2\pi r}\right)^{-1/2} \tag{2.7}$$

where $\lambda = c/f$ is the wavelength. The acoustic pressure obtained by either (2.6) or (2.7) is sometimes called the *pressure equivalent particle velocity* which justifies for the notation v_p in order to avoid confusion with the plain pressure field or the particle velocity field.

In the frequency domain the equivalents of (2.6) and (2.7) are (for axis x, as an example)

$$\begin{aligned} V_p(x,\omega) &= \rho c V(x,\omega) \\ &= \frac{\rho c}{j\omega} A(x,\omega) \\ &= \frac{\rho}{jk} A(x,\omega) \end{aligned} \tag{2.8}$$

and

$$\begin{aligned} V_p(x,\omega) &= \rho c V(x,\omega) \left(1 + \frac{\lambda}{2\pi r}\right)^{-1/2} \\ &= \frac{\rho c}{j\omega} A(x,\omega) \left(1 + \frac{\lambda}{2\pi r}\right)^{-1/2} \\ &= \frac{\rho}{jk} A(x,\omega) \left(1 + \frac{\lambda}{2\pi r}\right)^{-1/2} \end{aligned} \tag{2.9}$$

where (2.2) was used and the wavenumber $k = \omega/c$. In practice the measured accelerations are transformed to frequency domain using an FFT and then either (2.8) or (2.9) is applied to get $V_p(x,\omega)$, for the six acceleration channels (one along each axis). Note that dividing by $j\omega$ from acceleration to velocity implies a low pass filter with a slope of -20dB/decade showing an infinite gain at $\omega = 0$ and a gain 1 (0 dB) at $\omega = 1$. This low-pass filtering is somehow countered by the range dependent factor in (2.9) for short ranges. Considering a limit of 5% decrease and a range ≤ 7 m (which is the distance during Biocom'19, from the recorder to shore and to the sea surface), the range dependent factor should be used for frequencies ≤ 350 Hz. In order to avoid too large values for particle velocity pressure equivalent at low frequency the spectrum is clipped.

In this case sample spectrum (STFT), PSD and PS will be estimated using the relations and normalizations set out in [9].

2.3 Directional data analysis

Particle acceleration is measured along the three axes, so somehow it already provides directional information. This information can be combined to steer beams to any direction in the 3D space. In order to clarify ideas, figure 2.1 shows an orthogonal axis system with the orientation of the DAVS1 as it was deployed during the BIOCOM'19 experiment. As already mentioned the x-axis is pointing up, towards the sea surface, while the z-axis is pointing towards the rock pier. Since DAVS1 usual orientation (see Fig.1 in [8]) is rotated of 90 degrees in the $x - z$ plane, the angles θ and ϕ are maintained as bearing and elevation, respectively, but defined differently. Note that the two D separated 3-axial accelerometers are positioned along the z-axis, now horizontal pointing towards the rock pier. The received signals are termed V_{pz1} and V_{pz2} while the acoustic pressure sensor P is at the axes origin and the midpoint between the two accelerometers. There are several forms to combine the various channels: one is to combine pressure and particle velocity along the z-axis taking advantage of the two accelerometers dipole - this is the 1D array

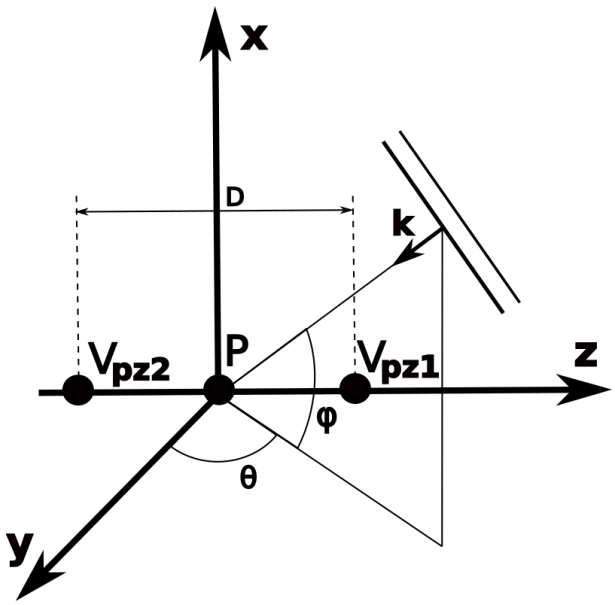

Figure 2.1: *diagram of plane wave in the DAVS1 axes system as installed during the BIOCOM'19 experiment.*

case; the other is to combine pressure and particle velocity along the three axis but for one accelerometer only - this is the single accelerometer 3D case; and finally the array 3D case where one attempts to use both accelerometers to steer beams in any direction, which will be left for future development.

2.3.1 Acelerometer 1D array case

Following the analysis in [8], adapted to the definitions of figure 2.1, one can write a combination between particle velocity pressure equivalent inputs at the two accelerometers with the midpoint acoustic pressure (in the frequency domain) as $\tilde{P}(\omega)$ such that

$$\begin{aligned} \tilde{P}(\omega) &= P(\omega) + V_{pz}(\omega), \\ &\approx P(\omega)(1 + \cos\phi), \end{aligned} \tag{2.10}$$

where the approximation stands for $\pi D \ll \lambda$. The figure of merit is a cardiod with the maximum along the z-axis ($\phi = 0°$), whose beamwidth at -3 dB is approximately 130°.

2.3.2 Single accelerometer 2D and 3D cases

The cardiod of (2.10) may be steered to any elevation ϕ by including the vertical x-axis

$$\tilde{P}(\omega, \phi) = P(\omega) + V_{px}(\omega)\sin(\phi) + V_{ph}(\omega)\cos(\phi), \tag{2.11}$$

where $V_{ph}(\omega)$ is simply the projection of the particle velocity (pressure equivalent) vector onto the horizontal $y - z$ plane. A three dimensional view may be obtained by including the expression of $V_{ph}(\omega)$ into (2.11) to get

$$\tilde{P}(\omega, \phi, \theta) = P(\omega) + V_{px}(\omega)\sin(\phi) + V_{py}(\omega)\cos(\phi)\cos(\theta) + V_{pz}(\omega)\cos(\phi)\sin(\theta). \tag{2.12}$$

The definitions of θ and ϕ are given in figure 2.1.

Alternatively, if only the steering angle is required, one may use the method proposed in [12] and, considering that the biological information to be estimated is uncorrelated and of much larger amplitude than the other ambient noise components (environmental and anthropogenic), obtain a θ bearing plane wave estimate as

$$\hat{\theta} = \arctan \frac{< p(t) v_{pz}(t) >}{< p(t) v_{py}(t) >} \approx \arctan \frac{\mathbf{u}_z}{\mathbf{u}_y}, \tag{2.13}$$

where $p(t)$ is the acoustic pressure, $v_{pz}(t)$ and $v_{py}(t)$ are the pressure equivalent particle velocity z and y sensor outputs, where $< \cdot >$ represents time average and stands for an estimate of the zero-lag cross-correlation, and where $\mathbf{u}_z$, $\mathbf{u}_y$ are unitary vectors along the respective axis. The previous relation also implicitely assumes that sensors along directions z and y have the same amplitude (or gain) and that they are colocated with the pressure sensor.

Chapter 3

Equipment and installation

The list of equipment used during the BIOCOM'19 sea trial contains four acoustic devices, a sound source and three bottom moored receivers, as well as other non-acoustic recorders such as an hand held CTD and several temperature and depth recorders placed both at the source and receiver locations.

3.1 Experiment area

The BIOCOM'19 experimental area is the Cabo Frio Island bay comprised between the Pontão da Atalaia main land and the island of Cabo Frio as shown in figure 3.1. The island of Cabo Frio is separated from the main land by the Boqueirão which is an opening of the rocky pier that extends from the Pontão da Atalaia, enclosing the bay on the southern side. The Boqueirão is an approximately 60 m wide inlet through which large masses of water get in and out of the bay. Due to the strong (mostly tidal) currents the water depth reaches 30 m at the center of the inlet while it has less than 10 m in most of the bay. Towards the north the bay opens to the Baia dos Anjos, island of Porcos and the northeastern passage. The bay is generally well protected but from northeastern winds which are predominant and sometimes very strong in the summer. These winds have two effects: one is to generate relatively high waves in the shallow area of the bay and, after a few days, to generate upwelling conditions on the south part of the Cabo Frio coast. Under these conditions, rising tide pushes cold water through the Boqueirão inlet into the bay. Figure 3.1 also shows the position of the acoustic source and receivers and the arrow represents the acoustic transmission line across the bay. The bottom in the area is mostly covered by a layer of fine sand with possible thinner layers, or even surfacing rocks, in the slopes near the Boqueirão inlet.

Figure 3.2 shows the approximate bathymetry along the transmission line with a simulation of the transmission loss at 8360 Hz, using the Bellhop model. At this frequency a significant part of the energy is lost in the first shallow portion of the transect while the acoustic signal crossing of the deep channel scrambles the arrivals that then arrive inchoerently at the receiver on the left most part of the figure. Is it anticipated that this significant and abrupt bathymetry variation together with the possible and probable water column temperature variation in the deepest part of the transect will pose significant difficulties for the accurate modelling of the propagation for applications such as tomography and/or source localization.

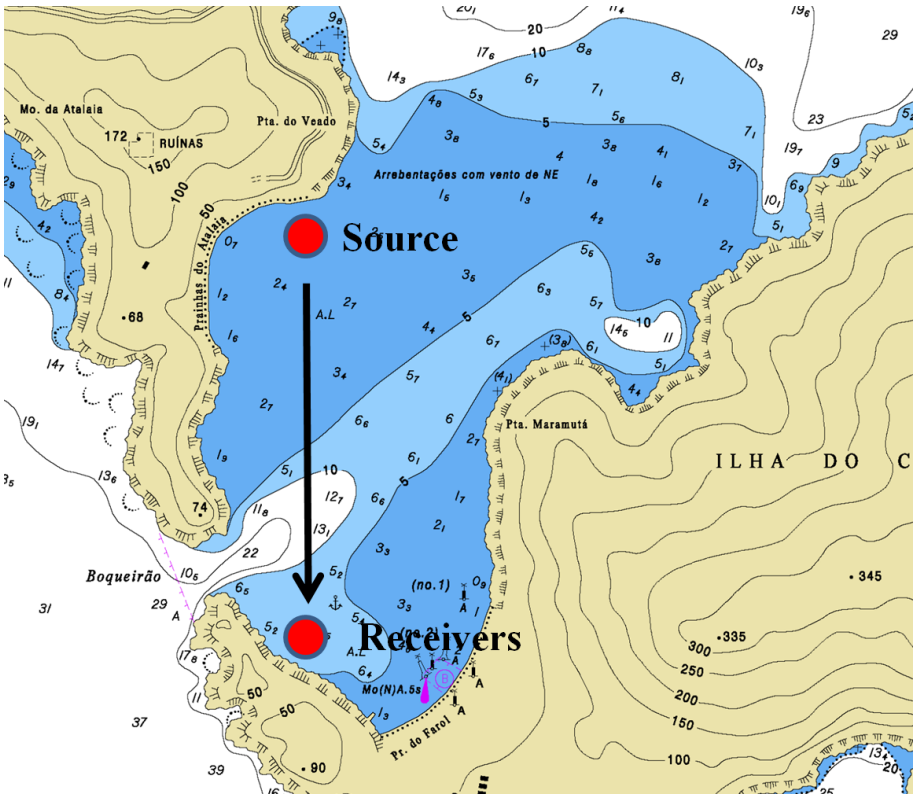

Figure 3.1: *BIOCOM'19 area with bathymetry, source - receiver positions and acoustic transmission path (from [1]).*

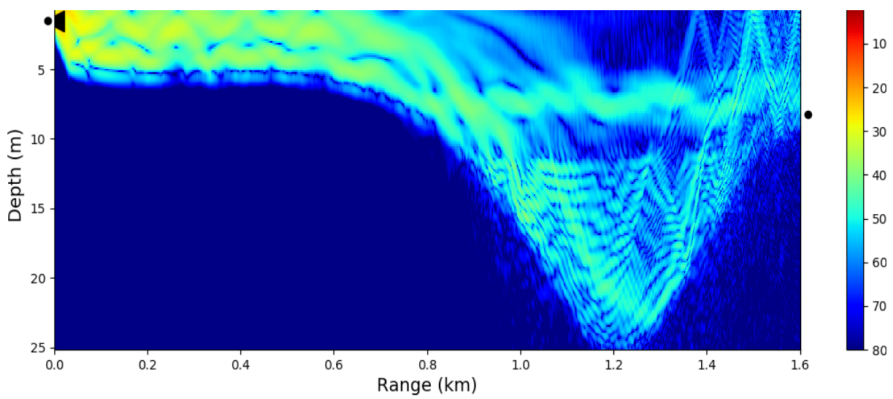

Figure 3.2: *bathymetry and simulated transmission loss at 8360 Hz, using the Bellhop model along the transmission line shown in figure 3.1 (from [1]).*

3.2 Non-acoustic equipment

Three types of non-acoustic equipment were used during the experiment:

- water level recorders, both on top of the source mooring and on top of the receiving array mooring
- temperature recorders: at the top of the source mooring, at the top of the vertical array mooring and at each array hydrophone

- CTD with sound velocity casts performed along the transect at various moments during the days of the experiment

3.2.1 Water level recordings

Water level recordings (see figure 3.3) both at the source and at the receiver locations, showed a tidal dependent in-phase variation increasing from 0.5 m at begining of the experiment, up to about 1 m at the end of the week.

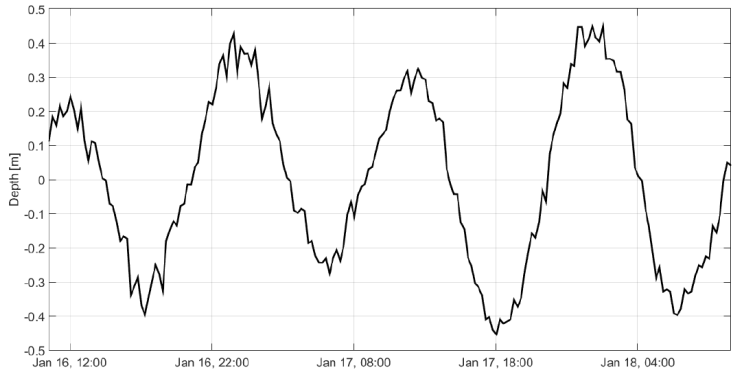

Figure 3.3: *water level variations at the receiver location (from [1]).*

3.2.2 Temperature recordings

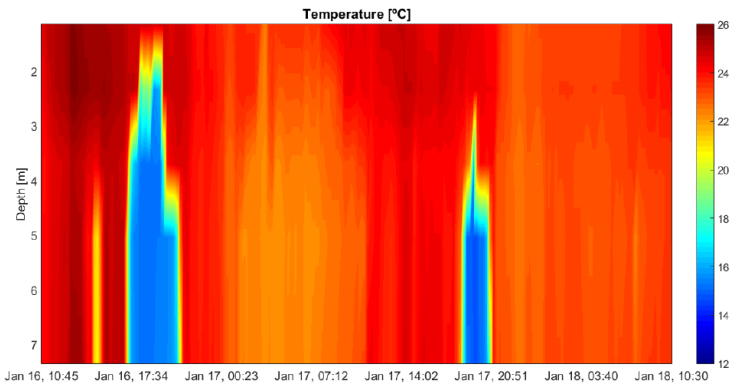

Figure 3.4: *temperature in °C recorded at the receiver location from January 16th to 18th, 2019 (from [1]).*

Temperature recordings at the top of the source and receiving vertical array moorings showed a diurnal oscillation between 22 and 24 °C. The four temperature recorders placed along the vertical line array showed an interesting behaviour with two strong oscillations in phase with the afternoon low tide on day January 16 and 17th, where the temperature varies abruptly from 24 to 14 °C in a few minutes (see figure 3.4). Most certainly, this cold water is entering through the Boqueirão and reaching the receiver position while staying between 2 a and 8m depth.

3.3 Acoustic equipment

3.3.1 Sound source

The sound source is an ITC sound projector model 1001 with an approximately omnidirectional transmitting pattern, a resonant frequency of 16.5 kHz at 149 dB // 1μPa/V @1m. The transmiting voltage response shows a relatively narrowband band at -3 dB between 14 and 16 kHz. At 2 kHz the voltage response is approximately -39 dB down from the peak value. The source was moored at mid depth in approximately 4 m of water and cabled to shore for power and signal command.

3.3.2 Acoustic receivers

The receivers are composed of a 4 hydrophone vertical line array, a 4-hydrophone tetrahedron shaped array sitting in the bottom (see picture in figure 3.5) and a dual accelerometer acoustic vector sensor (DAVS). This report will focus on the data gathered by the DAVS (see below).

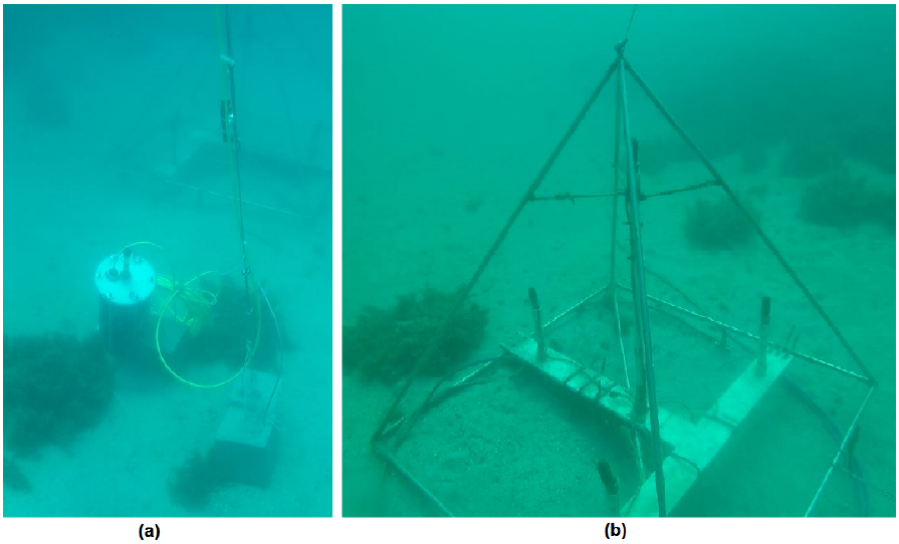

Figure 3.5: *the vertical line array (a) and the tetrahedron bottom sensors (b) at sea during the BIOCOM'19 sea trial (from [1]).*

3.3.3 DAVS1 installation and orientation

Since the DAVS1 is a directional device, keeping track of its orientation when at sea is important so a careful deployment and directional calibration was performed and described below. In the preliminary data analysis, sections 4.2 and 4.3, are dedicated to the description and then detection of active transmissions so noise periods could be automatically set apart for subsequent processing.

The DAVS1 was installed in a tripod stainless steel frame posed in the ocean bottom at approximate position (23.0088S, 42.0483W). A still picture taken from a movie done

during the installation is shown in figure 3.6. The DAVS1 is vertically positioned about 1 m above the sandy bottom: white tube with the black sensing element on top. The white box seen in the picture below the sensor itself is the battery extension. The distance from

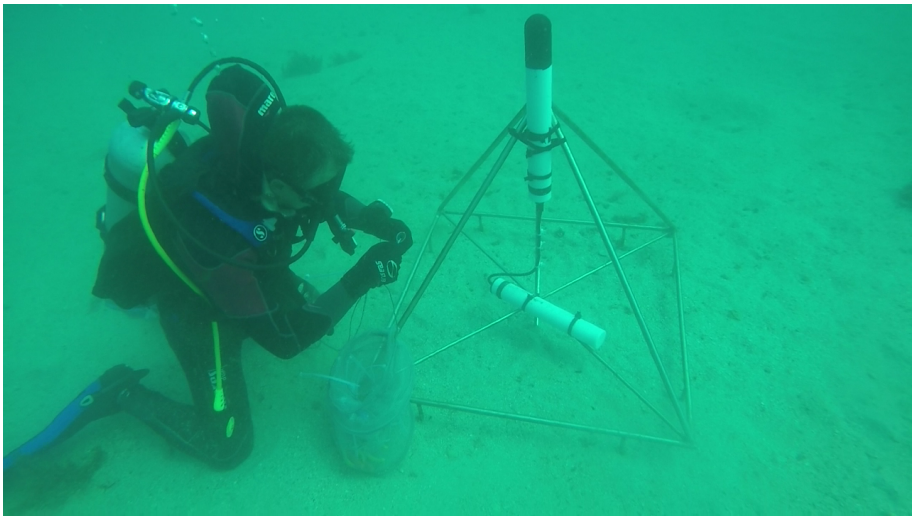

Figure 3.6: *picture taken during DAVS1 installation.*

the base of the rock shore is approximately 8 m, and the water depth at the location varies between 7 and 8 m. This position is circa 1.7 m to the NW of the BIOCOM tripod along a line parallel to the rock shore. According to the superimposed diagram on the area map shown in figure 3.7(a) the DAVS1 position is indicated by the red dot while the long arrows designate coordinate directions: 210 degrees to the rock shore and 310 degrees along the coastal area to NW. The DAVS1 axes reference system is shown in figure 3.7(b),

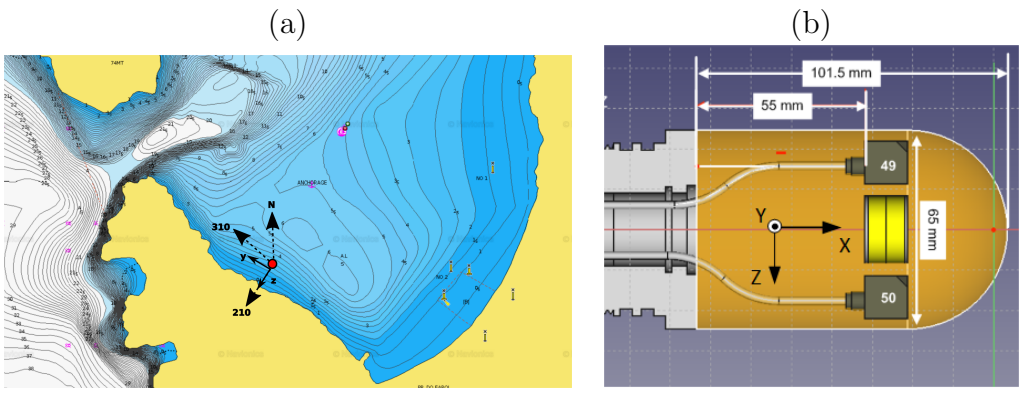

Figure 3.7: *diagram of the instrument position near the shore at Ilha de Cabo Frio (a) and a drawing of the internal reference axes system for the DAVS (b).*

while it is clear that for BIOCOM'19 the sensor is placed upright with the z-axis pointing to the rock shore and y-axis pointing at 90 degrees along the approximate rock shore direction. Accelerometer #50 is turned to the rock shore while #49 is on the opposite side, facing off the rock shore to the open bay. This information should be confirmed with the self recorded attitude data in section 4.1.

Chapter 4

Preliminary data analysis

Data analysis focus on the periods of the sea trial where the DAVS1 was active. Due to the shortage of battery modules for the required power consumption the DAVS1 was deployed and then recovered for battery charging and then redeployed. The first deployment took place on January 14th 10:30 UTC (8:30 local) and was recovered on January 16th at 11:00 UTC (9:00 local). The second deployment was made on the same day, January 16th at 18:00 UTC (16:00 local) and then finaly the device recovery on January 18th, 11:00 UTC (9:00 local). However, since the batteries were exausted well before the recovery, the recording intervals are shorter then the deployment period. The data intervals are as follows:

- Day1: January 14, 10:19 UTC to January 15 10:05 UTC
- Day2: January 16, 17:48 UTC to January 17 16:26 UTC

which correspond approximately to 24h recording for each deployment. We will refer to those two periods as Day1 and Day2.

It should be noted that local time in the Rio de Janeiro is normally UTC-3 but in the austral brasilian summertime, Day Saving Time (DST) is observed so, local time is UTC-2. It should also be noted that IEAPM TP1-4 equipment is running all year round in UTC-3. For reference sunset and sunrise times (in UTC-3) in Arraial do Cabo in January 2019 are given in appendix A.2.

There are actually three data types being recorded by DAVS1:

1. a set of attitude sensors for recording roll, pitch and heading, termed as r, p and h.
2. acoustic pressure field in one hydrophone, named as P
3. particle acceleration field sensed along three perpendicular axes, named as A_x, A_y and A_z, in two closely separate sensors, #49 and #50, one on each side of the hydrophone

Sensitivity and characteristics of the DAVS1 are given in annex A.1. For this experiment the programmable (linear) gain was set to PGA - hydrophone = 16 for the hydrophone and to PGA - accelerometer = 1 for the accelerometers. All the other values are fixed.

4.1 DAVS1 attitude data

Besides the physical placement of the DAVS1 as described above, the recorder has additional positioning sensors that are able to record movement variables such as roll, pitch and heading along time. This section reports the data gathered at those sensors. Although these variables are mainly for positioning correction during platform motion (the DAVS1 was designed for AUV mounting) they can also be used for verifying the above positioning coordinates / orientation.

Figure 4.1 shows roll, pitch and heading for the Day1 (a) and for Day2 (b). The first

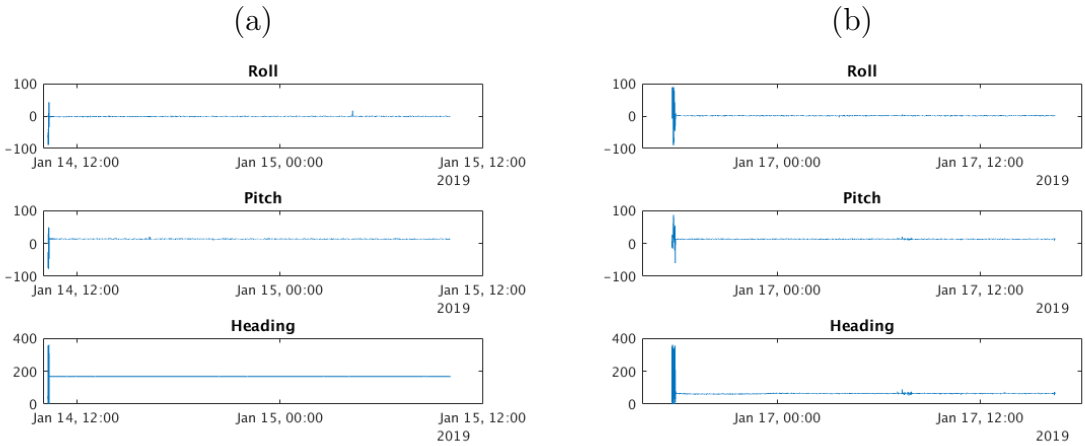

Figure 4.1: *DAVS attitude sensor recordings for roll, pitch and heading for Day1, January 14-15 (a) and for Day2, January 16-17 (b) (time UTC).*

remark is that apart for the initial values (probably recorded before deployment) the sensors show absolutely constant values throughtout the recording interval. While roll and pitch are at, or very close, to zero the heading takes a value of approximately 170 degrees for Day1 and about 65 degrees for Day2. The reading on Day1 compensated with 23° of magnetic declination at that latitude gives approximately 200 degrees which is very close to due 210 as shown in figure 3.7. The reading of 65 degrees for Day2 can not be understood, and it is not clear whether it is a malfunction or a lack of calibration of the sensor, or a real positioning error during deployment.

4.2 Active transmissions

As explained above, a sound source was transmitting pre-assigned codes at regular intervals. Figure 4.2 shows the schedule of transmission around one hour (a) and the content of each 5 min data pack (b). Max power transmissions at level SL start at minute 45 and repeat every 5 min until minute 15. From that moment on source level decreases 1 dB every 5min sequence repetition until last transmission at minute 40, where source level is 6 dB down from max power. The 5 min long transmit block repeated every 5 min is composed of four codes, Code 1 to Code 4, briefly described in table 4.1, and inter-spaced with 1 s of silence and then with a long period of 80 s of silence at the end, shown in a light green color in figure 4.2(b). These coded sequences were received in the recorders positioned in the proximity of the rock shore, including the DAVS1, after approximately 1.6 km signal propagation across the bay (see arrow transmission line in figure 3.1). Most

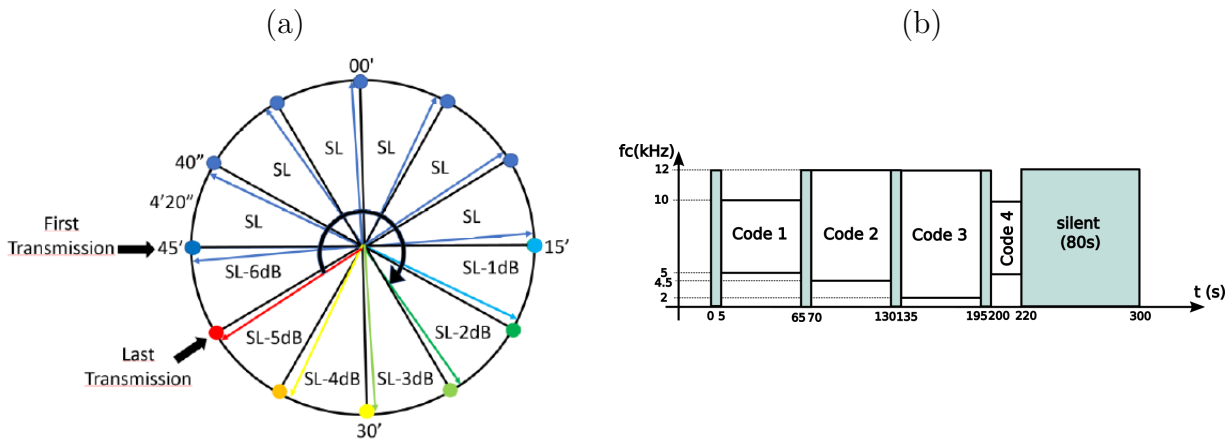

Figure 4.2: *acoustic source transmitting schedule (taken from [2] with permission) (a) and 5 min data pack content (b).*

Code/signal	duration (s)	band (kHz)
Code1 (Louza) BPSK	60	5 - 10
Code2 (Lussac) 8-CHSK	60	4.5 - 12.2
Code3 (Vale/Simões) LFM/CW	60	2 - 12
Code4 (Osowsky) 8-FSK	20	5 - 10

Table 4.1: *signal codes alignment on each 5 minute data packet. Names in () are those of the responsible persons for generating the coded sequences.*

of the transmitted codes were above the max cut-off frequency of ≈5 kHz of the DAVS1. However Code 3 does have LFM sequences transmitted below the 5 kHz max frequency and received in the DAVS1. As shown below these LFMs were detected and used for synchronization of the 80 s noise only periods at the end of each data packet, every 5 min. As we will see, in many cases, decreasing the source level around the hour will have an impact in the detection of the silent periods.

4.3 Noise periods detection

As mentioned above, the recorded acoustic data include seven channels as follows:

- two tri-axial accelerometers: #49 and #50, producing six information rich channels with acoustic particle accelerations, labelled as Ax49, Ay49, Az49, Ax50, Ay50 and Az50, in m/s^2.
- one acoustic pressure channel labelled Prs, in μPa.

The various channels where processed using the methods proposed in section 2. In a first step for the extraction of the bioacoustic information, this requires the detection of the noise periods, *i.e.*, those periods without active transmissions where anthropogenic free biological sound could be, in principle, recorded.

An example of spectrogram PSD of a 120 s recording obtained at 19:25 UTC (17:25 local time) on January 14, is shown in figure 4.3 where particle velocity channels Vx, Vy and Vz from accelerometer #49 are shown in equivalent pressure using (2.8) together with the acoustic pressure (bottom) expressed in dB // $1\mu\text{Pa}^2/\text{Hz}$. Linear Frequency Modulated

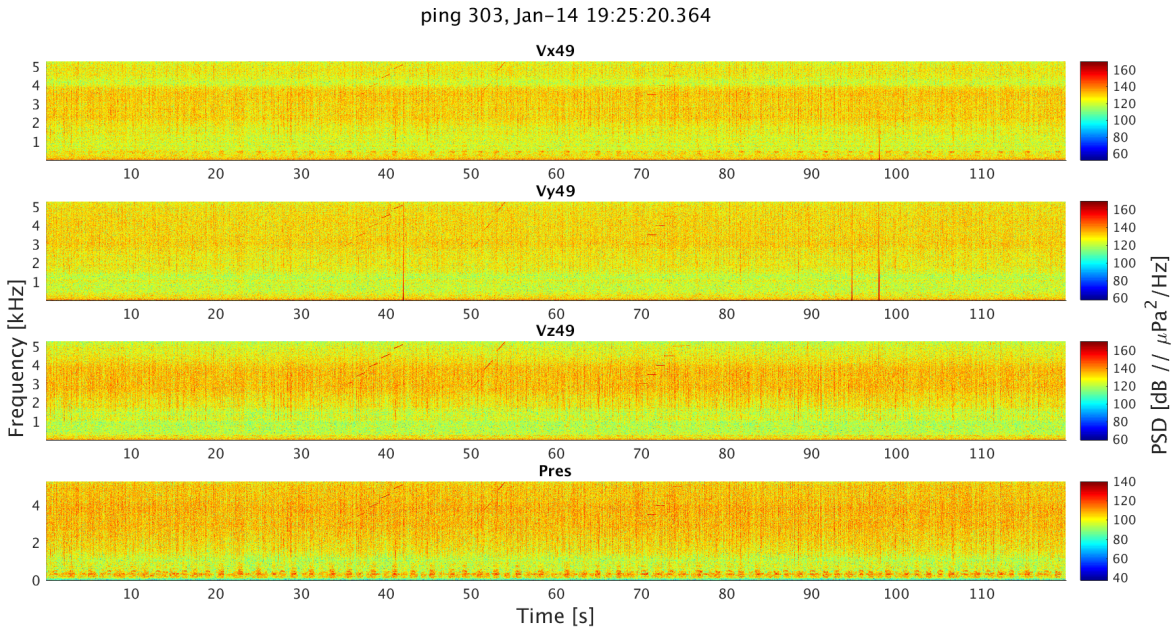

Figure 4.3: *PSD of received signals on (from top to bottom) Vx, Vy and Vz channels of accelerometer #49 and acoustic pressure, at start time 19:25:20.3 UTC of January 14, 2019.*

(LFM) signals can be clearly seen in all channels. These are the signals emitted bellow 5 kHz as part of the Code 3 sequence shown in the diagram of figure 4.4 and used for synchronization. Low frequency pulsed noise can be seen in the pressure and Vx channels and is inexistent in Vy an Vz. On the other hand Vx and Vy show a low noise band up to 1.5 kHz, and Vx and Vz show a clear noisy band between, say, 2 and 4 kHz. There are, however, clear differences among particle velocity channels and sound pressure. A correlator detector was performed for the 4.4-4.6 kHz one second duration LFM upsweep (red time-freq square on figure 4.4), which ouput is shown in figure 4.5(a) for the ping of figure 4.3 and the corresponding noise interval extracted using the correlation peak as reference. The spectrogram of the noise interval is shown in figure 4.5(b). Despite the low level of the signals received at that time, the LFM correlation gave a clear synchronization signal from which the source silent (noise only) interval could be time localized. The noise interval of 4.5(b) is apparently clear from anthropogenic interference, while there is low frequency noise (below 500 Hz) followed by a power decrease between 0.5 and 1.5 Khz and then a clear increase from that frequency on, possibly due to biological origin sound. The LFM detection process was repeated throughout the data. The detection intervals are shown in figure 4.6 for days January 14-15, and 16-17, 2019, in (a) and (b), respectively. It can be clearly noticed that no valid detection was obtained on the first day until late afternoon at around 18:00 UTC, while from then on a 5 min nearly constant interval was

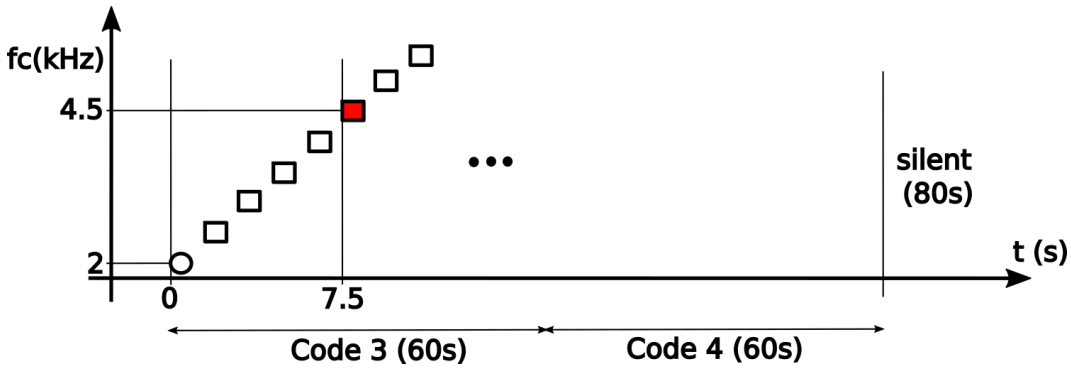

Figure 4.4: *detection sequence diagram: each LFM block has 1 s duration and 200 Hz bandwidth; block centered on 4.5 kHz at 7.5 s from start (in red) is detected and used for synchronization of the silent period.*

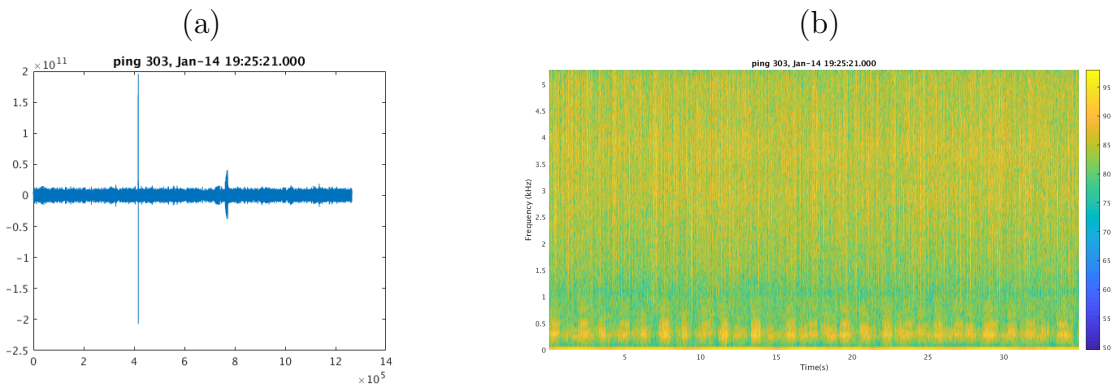

Figure 4.5: *4.4-4.6 kHz 1 s duration LFM correlation peak on ping 303 file of January 14, 2019, using the acoustic pressure channel (a) and the acoustic pressure 35 s noise interval extracted using that correlation peak as reference time (b).*

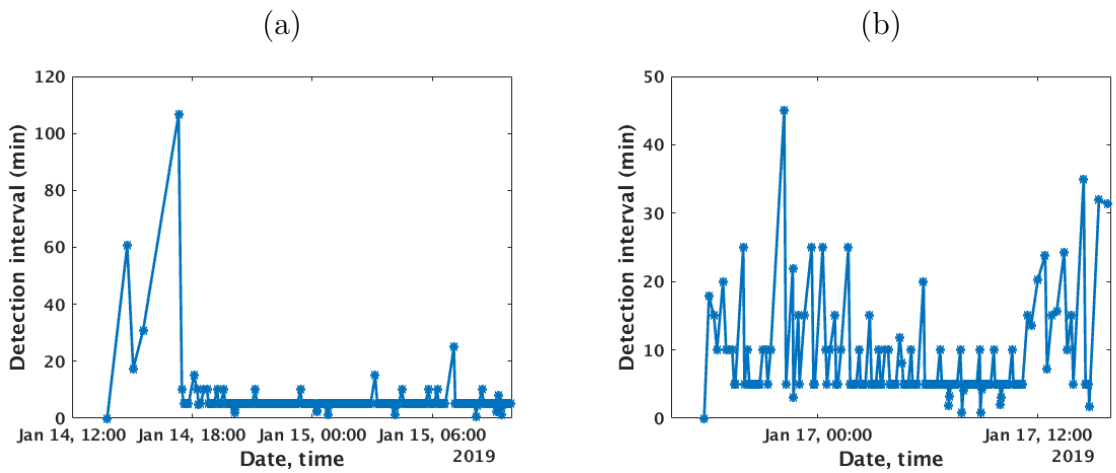

Figure 4.6: *detected intervals in minutes using the 4.4-4.6 kHz 1 second long LFM correlation peak along days January 14-15 (a) and January 16-17, 2019 (b).*

detected. On day 2, detection was more erratic fluctuating between 5, 10, 15 or 20 mins, possibly showing that there where missing sequences. This is more apparent late night on January 16, and then in the midday of January 17, by the end of the recording. Whether

that information can be correlated with transmission loss due to upwelling across the bay remains an open issue.

4.4 Acoustic pressure and pressure equivalent particle velocity

(I)

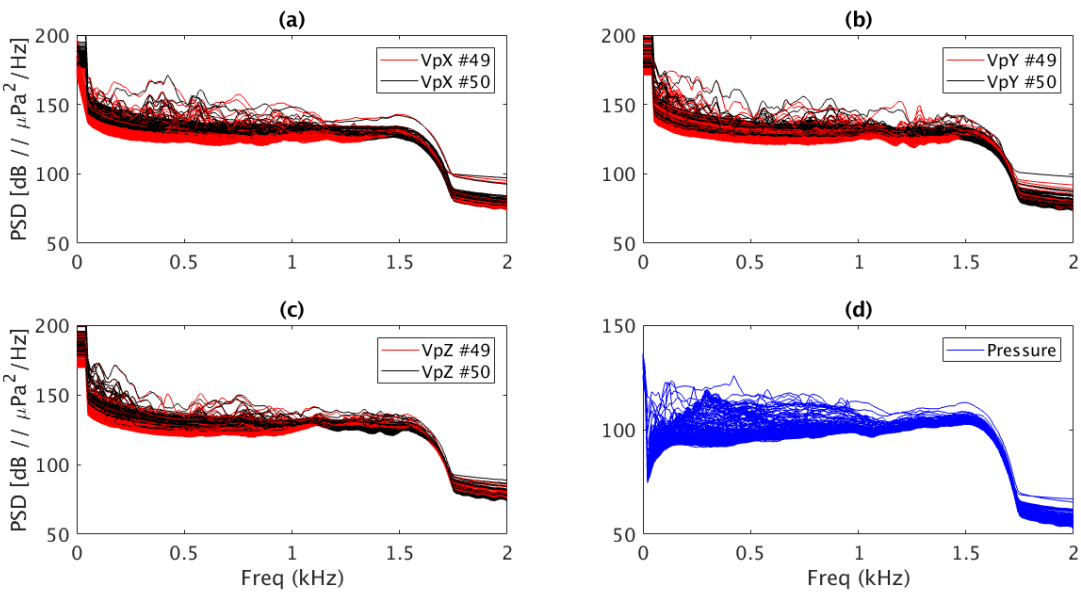

Figure 4.7: *noise spectra PSD for Day1, January 14-15 for the low-frequency band (I): pressure equivalent pressure channels x (a), y (b) and z (c) and pressure (d).*

After LFM synchronization and time selection, the power spectral density (PSD) of the received signals during the noise periods for day 1, January 14-15, are shown in figure 4.7 for the low-frequency band < 1.5 kHz (I) and for the high-frequency band, above that frequency (II). The following comments can be made:

1. power spectral densities of pressure channel at 90 - 110 dB, are always equal or lower than the corresponding pressure equivalent particle velocity, between 120 and 140 dB, or higher;

2. PSD levels in the LF band have a higher variability than in the HF band; this is particularly clear for the pressure field but also for the particle velocity where some packets show spurious peaks in the LF band; some of those extreme cases may be due to erroneous detection of the noise interval;

3. both for the LF and HF bands, Vpx and Vpy show a higher level for sensor #49 and lower for sensor #50, while component Vpz shows the opposite; this effect is clearer for the HF band;

4. in particular for the HF band in the x component Vp49 $>$ Vp50 while in the z component it is exactly the opposite and this difference increases with frequency, being more pronounced above 3 kHz.

(II)

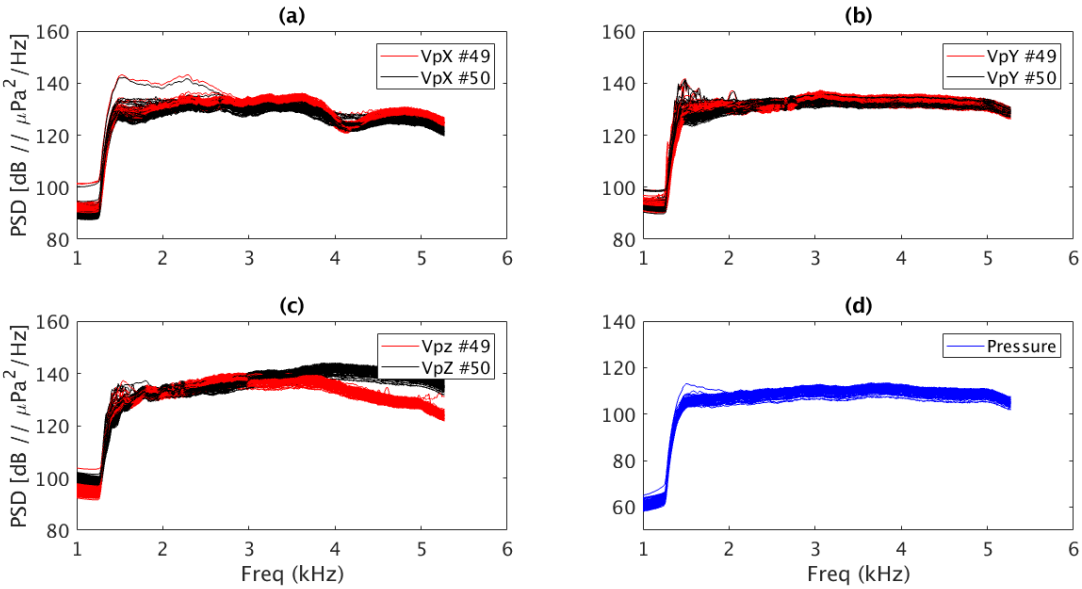

Figure 4.7: *noise spectra PSD for Day1, January 14-15 for the high-frequency band (II): pressure equivalent pressure channels x (a), y (b) and z (c) and pressure (d) (cont.).*

(I)

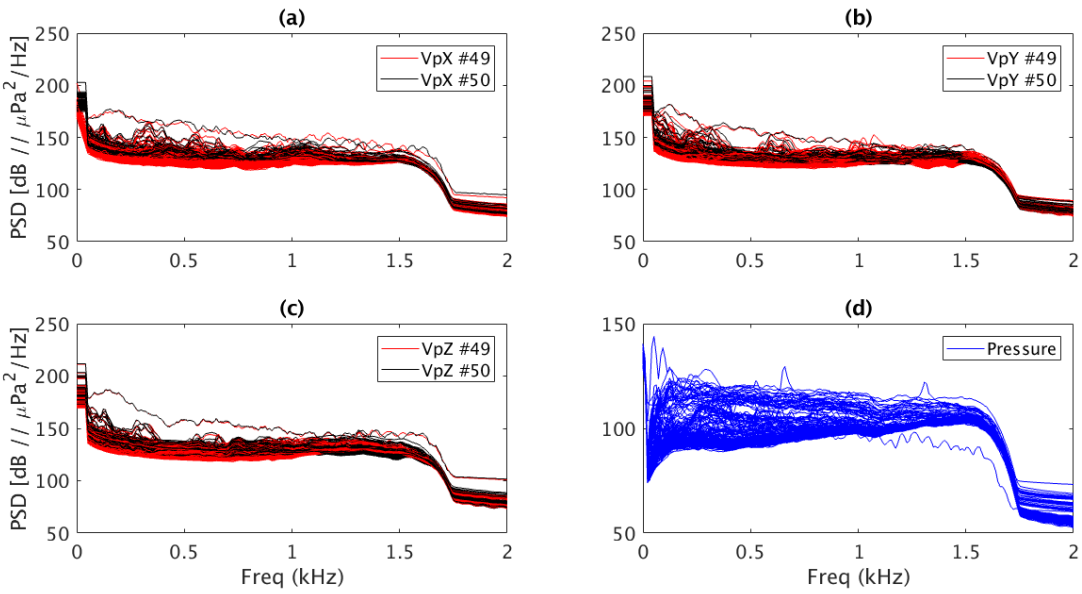

Figure 4.8: *noise spectra PSD for Day2, January 16-17 for the low-frequency band (I) : pressure equivalent pressure channels x (a), y (b) and z (c) and pressure (d).*

Similar plots for Day2, January 16-17, 2019, are shown in figure 4.8 for the low-frequency band < 1.5 kHz (I) and for the high-frequency band, above that frequency (II). The same comments as for Day1 apply, perhaps with an additional variation of the PSD below 3 kHz of the z component. Since the low frequency band (below 1.5 kHz) is mostly associated with anthropogenic noise a higher variability is expected, when boating occurs within acoustic reach of the receiver. Particle velocity levels' difference between the two

accelerometers may be explained by the fact that sensor #50 facing the rock shore shadows sensor #49 from the biological noise for z-axis , while the opposite is true for the other axis where open bay noise may be higher in sensor #49 facing the bay, than on sensor #50 facing the rock shore.

(II)

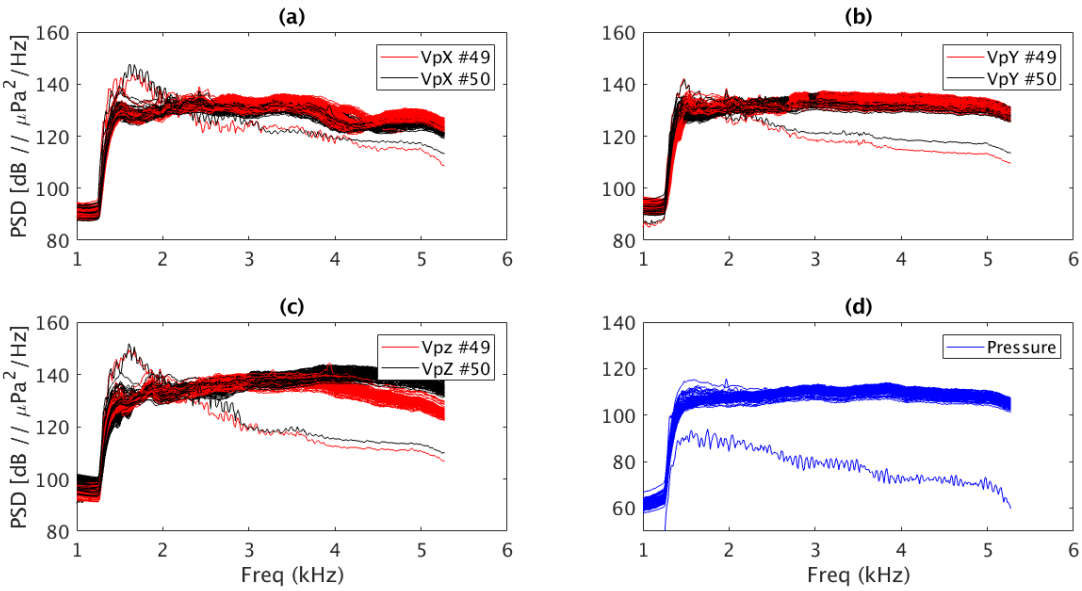

Figure 4.8: *noise spectra PSD for Day2, January 16-17 for the high-frequency band (II): pressure equivalent pressure channels x (a), y (b) and z (c) and pressure (d) (cont.).*

By summing the received noise power for each detected 70 s noise period over each recording day, separately for the two frequency bands (and normalizing by the bandwidth) one gets the total received power along time, as shown in figures 4.9 and 4.10 for days January 14-15 and 16-17, 2019, respectively. In the HF band, the pressure field clearly shows a biological signature with the peaks timely located before or at sun rise, and at just after sun set. These peaks can also be seen in the particle velocity channels with decreasing clarity from Vpz, Vpy and Vpx. The relative levels between the two accelerometers show the same inversion as in the previous figure, *i.e.*, higher levels for sensor #49 for channels Vpx and Vpy, and clearly lower levels for Vpz. We believe this may be explained by the already mentioned shadowing effect. The daily pattern has other spurious peaks in the channels Vpx and Vpy, for the time being, of unknown origin. On day2, January 16-17, the daily pattern is also present but not so clear as on day 14-15 (this might be due to the noise periods synchronization difficulties encoutered on that day). The levels' inversion between the various channels is maintained.

Percentiles are often used to give a perception of data dispersion. The percentile of PSD for acoustic pressure are shown in figure 4.11 for January 14-15 (a) and for January 16-17 (b). Clearly, median power spectral density is lower in the LF band (below 1.5 kHz) but has a much higher variability than in the HF band. This in line with the observations made above.

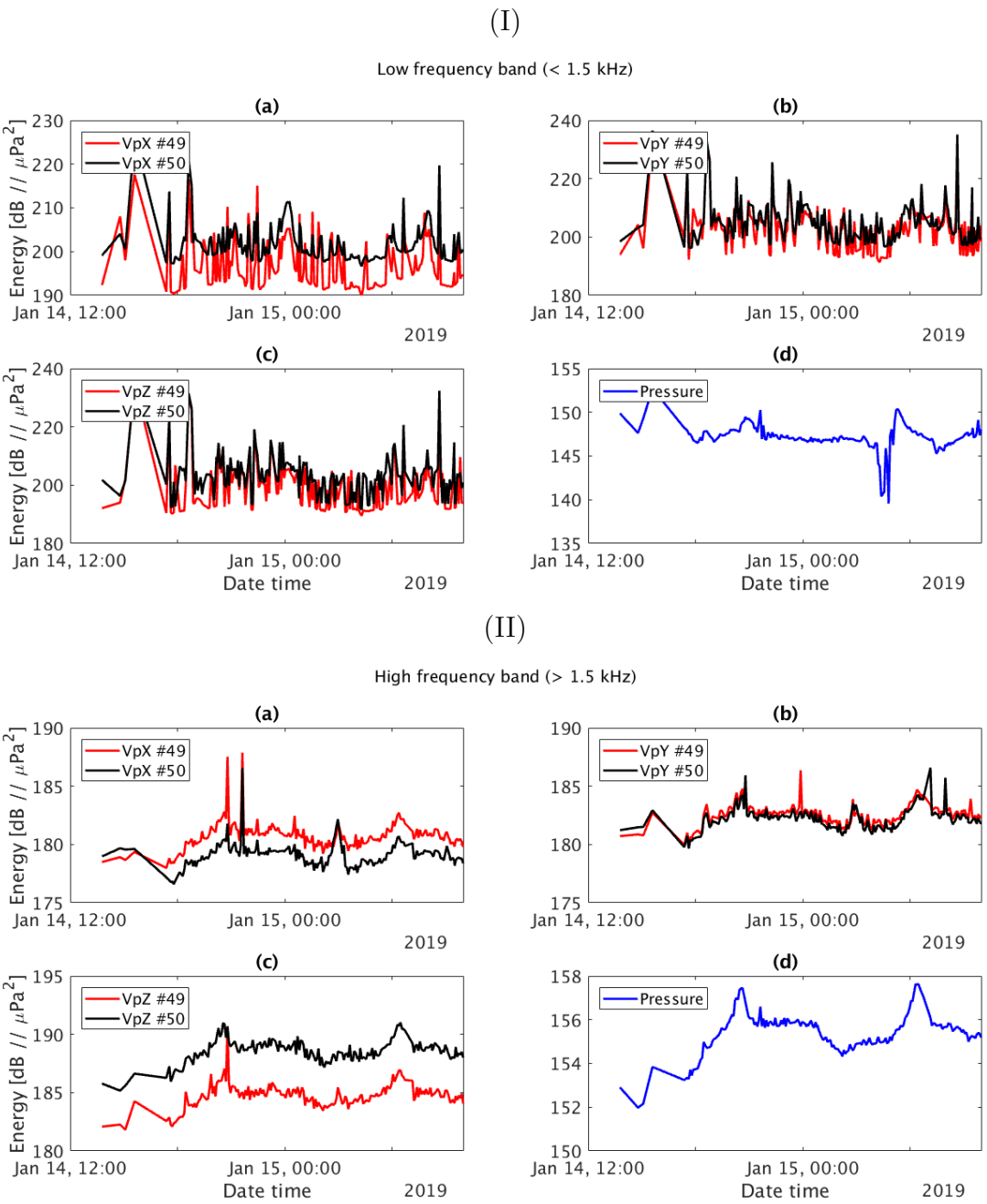

Figure 4.9: *total received power on the DAVS channels for day1 January 14-15 in the low frequency (I) and high-frequency band (II).*

4.5 Acoustic particle acceleration

Figure 4.12 shows the mean Power Spectral Density (PSD) calculated through the Welch method (also known as periodogram) in the 75 s noise periods of the detected data sequences for Day1 (January 14-15) and over the low frequency band 0 - 500 Hz. First, a Welch PSD is obtained for each 75 s interval using a sliding NFFT block size of 4096, corresponding to approximately 0.5 s, and a 50% overlap between data segments. Then an average of the PSDs over 12 consecutive noise blocks is performed with again a 50% overlap. If all consecutive 5 min sequences were detected, this would amount to roughly one hour of true data time on each PSD estimate so, due to the overlap, one time sample

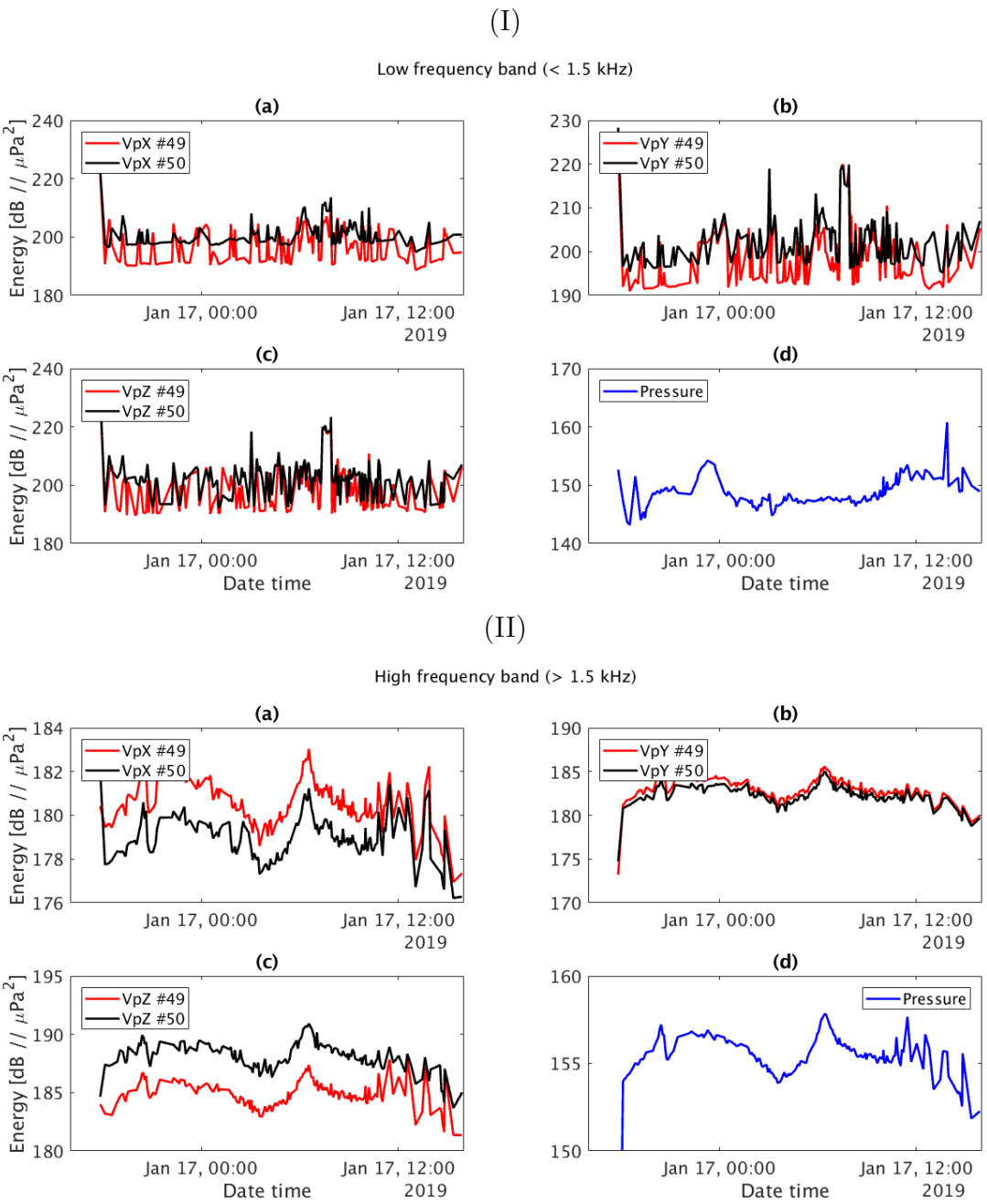

Figure 4.10: *total received power on the DAVS channels for day2 January 16-17 in the low frequency (I) and high-frequency band (II).*

was obtained every 6 new sequences so, every 30 min. The PSD is shown for the three axis X, Y and Z and for the two accelerometers #49 (left) and #50 (right). The pressure channel is also shown for reference. Acceleration is shown in $[(\mathrm{m/s^2})^2/\mathrm{Hz}]$ while pressure is in $[\mathrm{dB}\ //\ 1\mu\mathrm{Pa}^2/\mathrm{Hz}]$ (see color bars).

One can remark a significant sound pressure increase up to 120 dB, in the band above 150 Hz, peaking at 350 Hz until 22:00 UTC, i.e., 20:00 local time. The same levels seem to be picking up again in early morning at 09:00 UTC on January 15. The acceleration data shows its highest levels for low frequencies below 100 Hz, apart from a solitary peak at 400 Hz in the X axis (pointing up). There are strong time-frequency coincident peaks

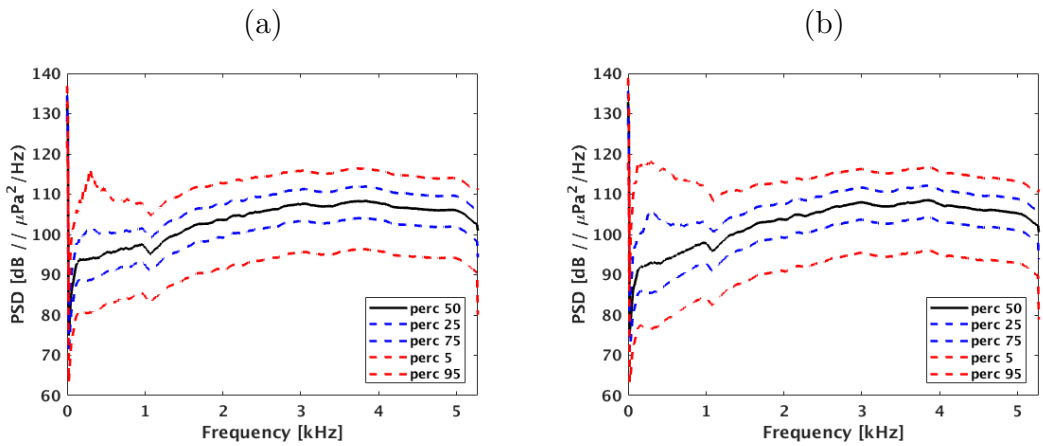

Figure 4.11: *acoustic pressure PSD percentiles for day January 14-15 (a) and January 16-17 (b).*

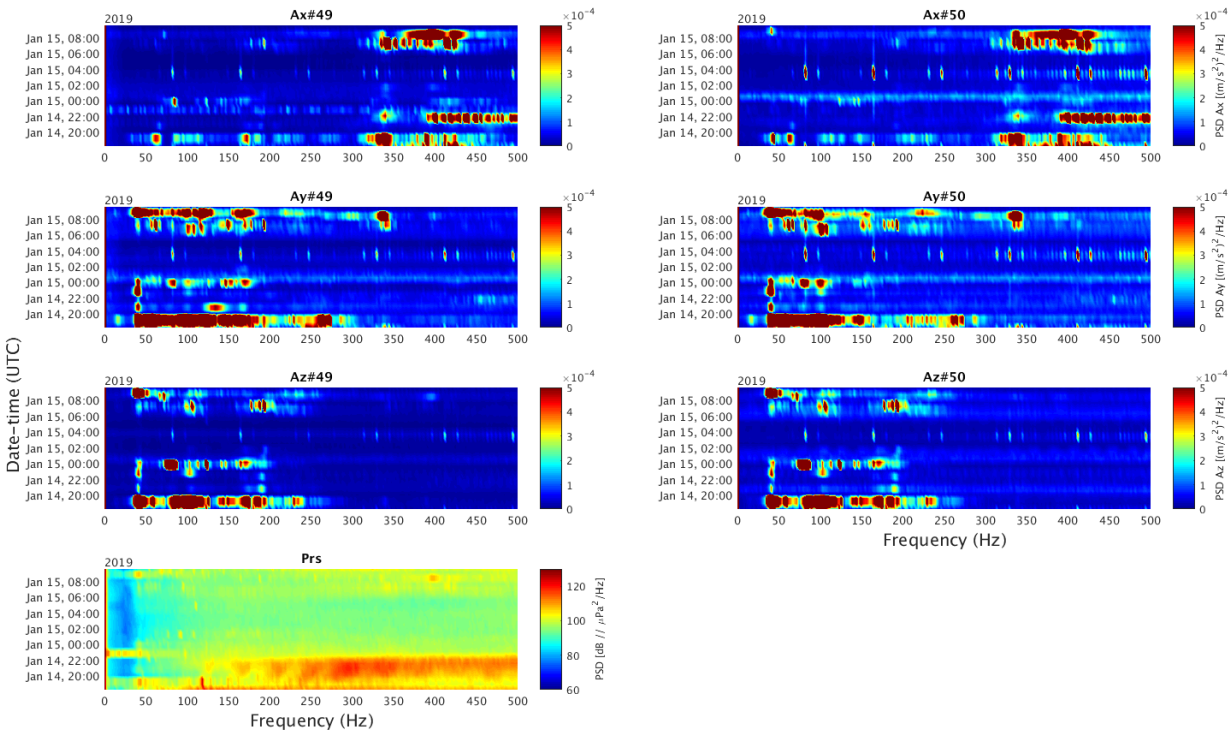

Figure 4.12: *received particle acceleration and pressure PSD for Day1, January 14-15, 2019: the three directional channels X, Y and Z for the two accelerometers #49 and #50, and the pressure channel (Prs).*

in the Y and Z axis at around 19:00 UTC on the 14th and then at 09:00 UTC on the 15. Remember that Y and Z point along and towards the rock shore, respectively. There is also a consistent night time spread increase of acceleration power density below 50 Hz in accelerometer #50, the one facing the rock and this is particularly relevant in Z axis, that pointing towards the shore.

Figure 4.13 shows the equivalent results for Day2 (January 16-17). Taking into account

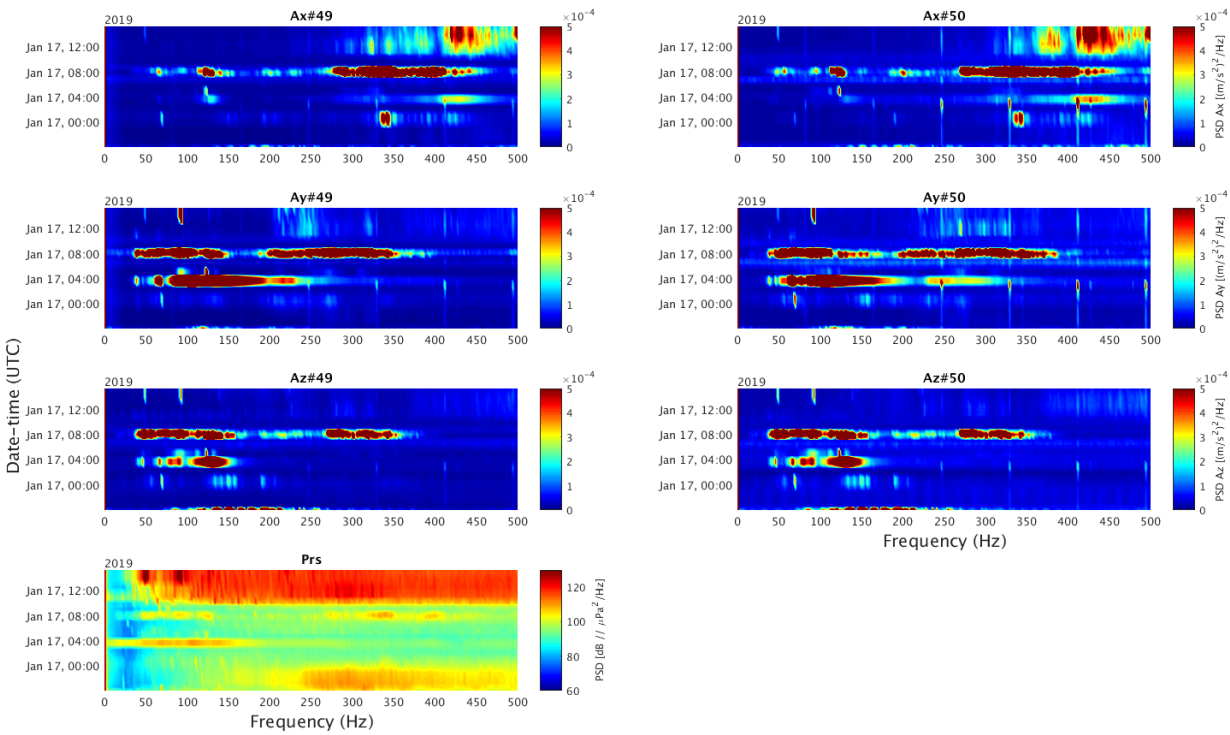

Figure 4.13: *received particle acceleration and pressure (for reference) PSD for Day1, January 16-17, 2019: the three directional channels X, Y and Z for the two accelerometers #49 and #50, and the pressure channel (Prs).*

the difference in date-time of the recording, the pattern is similar to that of Day1: pressure power increases in the morning (11:00 UTC, 09:00 local) with a possible arrival of boats in the area; a possible very close boat movement near the DAVS1 location at around 08:00 UTC (06:00 local) that can be seen on all axis but stronger in axis X and Y; a consistent night time spread increase of acceleration power density below 50 Hz in accelerometer #50, the one facing the rock and this is particularly relevant in Z axis, that pointing towards the shore.

If we take into account the close range approximation (2.9) for a range of $r = 7\,\mathrm{m}$, the acceleration is filtered through a function similar to that shown in figure 4.14(a) and its effect on the acceleration Az#49 PSD of January 16-17 at 20:02 UTC, is shown in figure (4.14)(b).

4.5.1 Acoustic directional data analysis

The next step is to extract directional information during the noise only periods. The various ways to do this are recalled in section 2.3, in particular those processors described in section 2.3.2, in relations (2.12) and (2.13), using angle definitions of figure 2.1.

The two figures 4.16 and 4.17, show the directional content of the acoustic field using the data received on Day1 and Day2, respectively. For each figure, plot (a) was obtained by taking the data received on one or the other accelerometer and the acoustic pressure

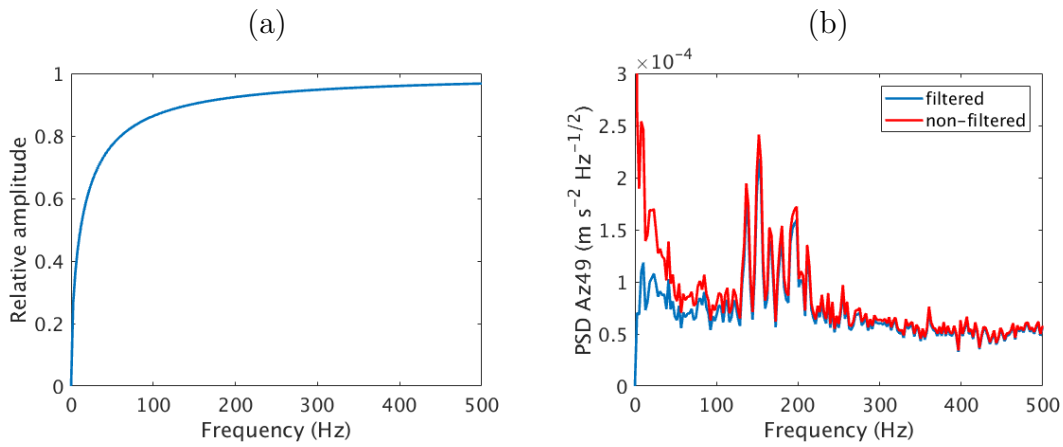

Figure 4.14: *short 7 m range low-frequency filter function (a) and effect on PSD of accelerometer data of Az#49 of Day2, January 16-17, 2019 at 20:02 UTC (b).*

and filter them through a 1.5 kHz high-pass FIR filter, as that used in section 4.4. Then, to compute the respective spectrum density field over a 75 s ping and combine using (2.12) for bearing $\theta \in [0, 360]$ and elevation $\phi \in [-90, 90]$, using the angle definitions of figure 2.1. Note that bearing 0 degrees points towards axis y, *i.e.*, approximately parallel to the rock pier, 90 degrees points to the rock pier, and so on. Elevation -90 degrees point to the bottom, and 90 degrees to the surface. From the obtained bearing - elevation surfaces the absolute maxima was selected and plotted along time ping. An example of such bearing elevation surface at the end of Day1 is shown in figure 4.15. One can notice that there are

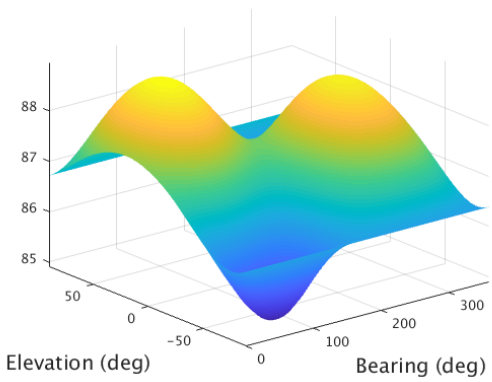

Figure 4.15: *day 1, January 14-15, bearing - elevation surface at the end of the period using accelerometer #49.*

two distinct main directions of energy arrival, one pointing to the rock pier and another pointing towards the open bay. The one pointing toward the rock pier has always shown a higher field intensity than the other, throughout the two analyzed periods.

In figures 4.16 and 4.17, plot (b) is obtained using (2.13) that assumes high SNR for the signal of interest in order to obtain an estimate of signal bearing only using, components y and z of each accelerometer (together with the pressure field). The results for Day1, January 14-15, show that bearing estimates coincide at around 80 degrees, thus pointing to the rock pier, for both accelerometers, with an estimate through time that is slightly more noisy for #49, the accelerometer on the bay side, than for accelerometer #50, the one on the rock pier side. Elevation is estimated approximately 25-30 degress for #49 and

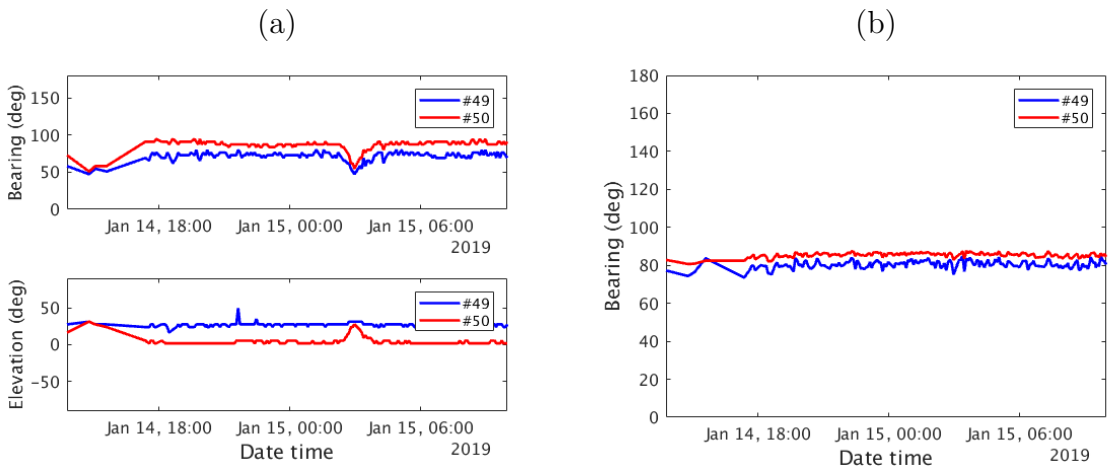

Figure 4.16: *day 1, January 14-15, bearing and elevation estimates for accelerometers #49 and #50 (a) and only for bearing (b).*

around 0 degrees (horizontal) for #50. This difference is probably due to the fact that #50 is directed towards the direct path of biological noise generated on the rock, while #49 is directed towards a surface reflection of it, also because it is shadowed by #50. The results for Day2, January 16-17, show very similar results to those of the previous

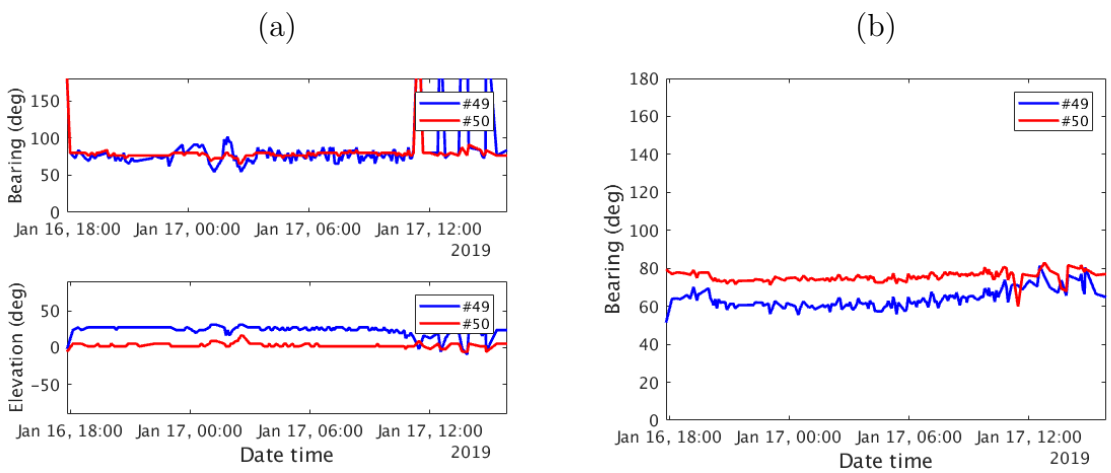

Figure 4.17: *day 2, January 16-17, bearing and elevation estimates for accelerometers #49 and #50 (a) and only for bearing (b).*

day with, however, a much larger degree of strong interference, specially in the mid day of January 17, prior to recovery, which was already noticed in the previous analysis. The estimated bearing is also slightly different from that of Day1, which is understandable since the receiver was recovered and redeployed in between and the alignment might be different.

Chapter 5

Conclusion

This report describes the usage of the particle motion recorder Dual Acoustic Vector Sensor (DAVS1) during the underwater communications experiment BIOCOM'19, carried out by IEAPM (Brazilian Navy) in the bay of Cabo Frio, Arraial do Cabo (RJ, Brasil) on the period January 14 - 18, 2019. Previous long term (1 year) soundscape recording in the area showed a strong biological signature, most apparent during the night periods, and an intense anthropogenic activity due to touristic boats and beaching related actitivities during day time (specially during the summer period). It was also shown that the bay is prone to an intense inflow of very cold water arising under upwelling conditions, through the narrow Boqueirão inlet, in synchro with the tide.

The scientific objectives of the experiment were twofold: 1) to analyse the particle motion level through recordings of the biological activity in the vicinity of the rock shore where a strong community of invertebrates and somniferous fish settle, and 2) to measure particle motion levels due to anthropogenic activities, eventually comparing to sound exposure levels of the various species. This report describes the experiment and gives an initial assessment of the DAVS1 data, revealing some hints for posterior analysis.

Approximately two days worth of data were recorded with DAVS1, from which 340 $\times$ 75 s long intervals of noise only where extracted to support objective 1). Preliminary results show that a) pressure equivalent particle velocity levels are at least 10 dB higher than those of sound pressure; b) those incresead levels are apparently linked to biological activity in the rock shore community; c) clear daily patterns can be seen on the horizontal channels of the DAVS1 in phase with those received on the acoustic pressure channel.

From the same two days recording periods of high variability and intense particle velocity pressure equivalent levels were recorded in the low-frequency band, possibly connected with anthropogenic activity, which may be used to support objectie 2), above. In cases, they appear to be higher than allowed sound exposure levels for some fish species, at least for short periods of time. Analysis of the particle acceleration data in the band below 500 Hz show spurious peaks and high levels not connected with the pressure field that may required further analysis.

Bibliography

[1] Equipa BIOCOM. Construção de métodos de sinalização com características de ruído bioacústico para comunicação submarina (biocom'19). Sea Trial Report JAN/19 - DAS, IEAPM, Arraial do Cabo (RJ, Brasil), Fevereiro 2019.

[2] R. Calazan, V.J. Barroso, M.V. Sim oes, and S.M. Jesus. Upwelling effect on acoustic propagation in the cabo frio island bay. In *Int. Conference on Acoustics - ICA'2019*, September 2019.

[3] A. Banner. Measurements of the particle velocity and pressure of the ambient noise in a shallow bay. *J. Acoust. Soc. America*, 44(6):1741–1742, 1968.

[4] G.R. Potty, M. Tazawa, J. Giard, J.H. Miller, Y-T Lin, A. Newhall, and K.J. Vigness-Raposa. Measurements of particle motion near the seafloor during construction and operation of the block island wind farm. In *Proc. Meeting Acoust. Soc. America*, volume 141, page 3993, 2017.

[5] P. Sigray and M. Andersson. Particle motion measured at an operational wind turbine in relation to hearing sensitivity in fish. *J. Acoust. Soc. America*, 130(1):200–207, July 2011.

[6] A.N. Popper and A.D. Hawkins. The importance of particle motion to fishes and invertebrates. *J. Acoust. Soc. America*, 143(1):470–488, 2018.

[7] A. Mantouka, P. Felisberto, P. Santos, F. Zabel, M. Saleiro, S.M. Jesus, and L. Sebasti ao. Development and testing of a dual accelerometer vector sensor for auv acoustic surveys. *Sensors*, 17(6):1328, June 2017.

[8] P. Felisberto, P. Santos, and S.M. Jesus. Acoustic pressure and particle velocity for spatial filtering of bottom arrivals. *IEEE Journal of Oceanic Engineering*, 44:179–192, January 2019.

[9] S.M. Jesus. Acoustic pressure and particle motion power spectrum estimation with matlab. Report 03/19 - SiPLAB, CINTAL, University of Algarve, 8005-139 Faro (Portugal), October 2019.

[10] H. Schmid. How to use the fft and matlab's pwelch function for signal and noise simulations and measurements. Report, Institute of Microelectronics, University of Applied Sciences, Northwestern Switzerland, August 2012.

[11] S.L. Nedelec, J. Campbell, A.N. Radford, S.D. Simpson, and N.D. Merchant. Particle motion: the missing link in underwater acoustic ecology. *Methods in Ecology and Evolution*, 7:836–842, 2016.

[12] P. Felisberto, J. Schneiderwind, P. Santos, O. Rodriguez, and S.M. Jesus. Comparing the resolution of bartlett and mvdr processors for bottom parameter estimation using pressure and vector sensor short array data. In IEEE, editor, *Proc. Oceans - Bergen, 2013 MTS/IEEE*, pages 1–8, Bergen, Norway, June 2013.

Appendix A

Appendix name

A.1 DAVS1 main characteristics

These are the main characteristics of the DAVS1 recorder as drawn from [7].

Table A.1: *DAVS1 system specifications*

Item	Description
Full experimental system	vector sensor, autonomous acquisition system
Cable length - existing / maximum	20 meters / 100 meters
Autonomy	battery, 20h (with 20V@3100mAh)
	cable connected, infinite (uses 24VDC)
Bandwidth	0.1kHz - 4kHz
RX elements	2x triaxial accelerometers, 1 hydrophone
Accelerometer	2x PCB 356A17 accelerometers IEPE type
	sensitivity 500mV/g
Hydrophone	cylindrical ceramic element
	sensitivity -195 dB re μ Pa/V
A/D channels	7 (simultaneous sampling)
A/D converter	24 bits Sigma Delta
A/D converter sensitivity	± 2.5 volts (full scale)
A/D sampling rates	10547sps / 52734sps
Storage capacity	dual 128GB microSD cards (expandable)
Time synchro	Local RTC, Local RTC or host (streaming)
Real-Time Clock	maintains accuracy at 1 second / month
eCompass	Roll, Pitch and Azimuth
	accuracy: ±1deg azimuth, ±45deg roll or pitch
	±2deg roll and pitch accuracy
Telemetry & Ethernet	(raw data and configuration)
Container size (diameter&length)	6.5cm / 50cm
Equipment weight	1.4kg outside and approx neutral in water
Maximum operating depth	10m

A.2 Sunset - sunrise times at Arraial do Cabo

.

ON OBSERVATÓRIO NACIONAL

Anuário Interativo do Observatório Nacional

Crepúsculo do Amanhecer e Anoitecer

Ano 2019 d.C.

Localidade: ARRAIAL DO CABO - RJ
Longitude: 42:01:40
Latitude: -22:57:58
Altitude (m): 1171

Fuso horário: -3

No horário de verão adicione 1h ao valor listado

Explicações

Janeiro									Fevereiro								
		Alvorada				Crepúsculo					Alvorada				Crepúsculo		
Dia	Nascer	Civil	Náut.	Astr.	Ocaso	Civil	Náut.	Astr.	Dia	Nascer	Civil	Náut.	Astr.	Ocaso	Civil	Náut.	Astr.
1	05:06	04:41	04:11	02:43	18:38	19:03	19:33	21:01	1	05:28	05:04	04:36	03:15	18:36	19:00	19:28	20:48
2	05:07	04:42	04:12	02:44	18:38	19:03	19:33	21:01	2	05:29	05:05	04:37	03:17	18:35	18:59	19:27	20:47
3	05:08	04:43	04:13	02:45	18:38	19:03	19:33	21:01	3	05:30	05:06	04:37	03:18	18:35	18:59	19:27	20:46
4	05:08	04:43	04:13	02:46	18:38	19:03	19:33	21:01	4	05:30	05:06	04:38	03:19	18:34	18:58	19:26	20:45
5	05:09	04:44	04:14	02:46	18:39	19:04	19:34	21:01	5	05:31	05:07	04:39	03:20	18:34	18:58	19:26	20:45
6	05:10	04:45	04:15	02:47	18:39	19:04	19:34	21:01	6	05:32	05:08	04:40	03:21	18:33	18:57	19:25	20:44
7	05:10	04:45	04:16	02:48	18:39	19:04	19:34	21:01	7	05:32	05:08	04:41	03:22	18:33	18:56	19:24	20:43
8	05:11	04:46	04:16	02:49	18:39	19:04	19:34	21:01	8	05:33	05:09	04:41	03:23	18:32	18:56	19:24	20:42
9	05:12	04:47	04:17	02:50	18:39	19:04	19:34	21:00	9	05:33	05:10	04:42	03:24	18:32	18:55	19:23	20:41
10	05:13	04:48	04:18	02:51	18:39	19:04	19:34	21:00	10	05:34	05:11	04:43	03:25	18:31	18:55	19:22	20:40
11	05:13	04:48	04:19	02:52	18:39	19:04	19:34	21:00	11	05:35	05:11	04:43	03:26	18:31	18:54	19:22	20:39
12	05:14	04:49	04:20	02:53	18:39	19:04	19:34	21:00	12	05:35	05:12	04:44	03:27	18:30	18:53	19:21	20:38
13	05:15	04:50	04:20	02:54	18:39	19:04	19:34	20:59	13	05:36	05:12	04:45	03:28	18:29	18:53	19:20	20:37
14	05:15	04:51	04:21	02:55	18:40	19:04	19:34	20:59	14	05:36	05:13	04:46	03:29	18:29	18:52	19:19	20:36
15	05:16	04:51	04:22	02:57	18:39	19:04	19:34	20:59	15	05:37	05:14	04:46	03:30	18:28	18:51	19:19	20:35
16	05:17	04:52	04:23	02:58	18:39	19:04	19:33	20:58	16	05:38	05:14	04:47	03:31	18:27	18:51	19:18	20:34
17	05:18	04:53	04:24	02:59	18:39	19:04	19:33	20:58	17	05:38	05:15	04:48	03:32	18:27	18:50	19:17	20:33
18	05:18	04:54	04:24	03:00	18:39	19:04	19:33	20:57	18	05:39	05:16	04:48	03:33	18:26	18:49	19:16	20:32